Optimization of two-dimensional ion trap arrays for quantum simulation

James D Siverns, Seb Weidt, Kim Lake, Bjoern Lekitsch, Marcus D Hughes and Winfried K Hensinger[1]

Department of Physics and Astronomy, University of Sussex,
Brighton BN1 9QH, UK
E-mail: W.K.Hensinger@sussex.ac.uk

Abstract. The optimization of two-dimensional (2D) lattice ion trap geometries for trapped ion quantum simulation is investigated. The geometry is optimized for the highest ratio of ion–ion interaction rate to decoherence rate. To calculate the electric field of such array geometries a numerical simulation based on a 'Biot–Savart like law' method is used. In this article we will focus on square, hexagonal and centre rectangular lattices for optimization. A method for maximizing the homogeneity of trapping site properties over an array is presented for arrays of a range of sizes. We show how both the polygon radii and separations scale to optimize the ratio between the interaction and decoherence rate. The optimal polygon radius and separation for a 2D lattice is found to be a function of the ratio between radio-frequency (rf) voltage and drive frequency applied to the array. We then provide a case study for ^{171}Yb$^+$ ions to show how a 2D quantum simulator array could be designed.

[1] Author to whom any correspondence should be addressed.

IOP Institute of Physics   Φ DEUTSCHE PHYSIKALISCHE GESELLSCHAFT

Contents

1. Introduction

Trapped ions possess long lived addressable internal states and can be highly decoupled from their environment. This makes them an important tool in the development of quantum information processing [1, 2] and quantum simulation [3–7]. When used for quantum simulation they enable complex spin systems, among others, to be investigated beyond the practical limitations of classical computation. For example, trapped ions have been used for quantum simulations of the evolution of paramagnetic into (anti-)ferromagnetic order in a spin system, [8, 9] and frustrated anti-ferromagnetic Ising interactions [10, 11]. These first simulations were carried out using one-dimensional trapping arrays and state dependent forces applied using laser beams.

More complex simulations will require ions trapped in two-dimensional (2D) arrays and interaction schemes compatible with these. Advances towards 2D trapping arrays suitable for quantum simulations have been made by trapping ions in a millimetre-scale mechanically fabricated metal mesh [12] and by the successful implementation of microfabrication techniques for ion traps [13]. In addition, interaction schemes based on large oscillating or static magnetic field gradients have been proposed [14, 15] and demonstrated in an on-chip microwave gate [16, 17]. With the recent advances in the field, ion trap quantum simulations using large scale 2D ion trap lattices are within the reach of current technology.

In order to create a 2D array of trapped ions a repeating 2D surface geometry is required. Decoherence due to anomalous heating is a major issue for large scale quantum simulations. As this heating scales approximately as r^{-4} [18], where r is the ion height above the trapping surface, it is advantageous for ions to be trapped high above the surface. However, when individual surface microtraps are placed together so that their separation is less than around twice the ion height the individual electric fields start to overlap and distort the resulting trapping fields [19]. In extreme cases this can lead to the traps combining to produce a singular trapping zone. To compensate for this the electrode structure has to be altered when operating within this regime [19]. Schmied *et al* [19] have investigated surface-electrode geometries and developed an algorithm that optimizes geometries to maximize the electric field curvatures of individual trapping sites for arbitrary ion heights and separations. Individual trapping sites shown in [19, 20] were optimized using this algorithm leading to non-intuitive electrode patterns which can contain many isolated radio-frequency (rf) and static voltage electrodes. Another proposal [21] working outside this regime uses rf electrodes with controllable rf voltages to lower trap frequencies and decrease ion–ion distances and, therefore, increase interaction strengths. However, this requires the use of multiple independent rf electrodes and individually controllable rf voltages posing an additional experimental complication.

In this paper we present an optimization process for ion trap topologies based on a single rf electrode island, reducing the requirement for buried rf wires and multiple rf electrodes. We focus on the development of an optimum lattice geometry where the ratio of coupling rate to the decoherence rate due to ion heating is maximized and made homogeneous across the lattice. This is achieved by minimizing the secular frequencies of the trapping sites whilst, simultaneously, keeping the trapping depths above a minimum trap depth (for illustrative purposes we use 0.1 eV) to allow for successful operation of the proposed 2D lattice designs. We will concentrate on the optimum lattice topology for hexagonal, square and centred rectangle lattices. An investigation is also carried out on how optimal geometries depend on the overall lattice size, and we discuss the choice of and scaling for experimental parameters such as rf voltage, drive frequency, ion mass and electric field noise density.

Additionally it is possible that 2D ion arrays of this type could also be used for quantum computation. For example, cluster state quantum computation could be carried out in such a system [22, 23]. However, additional constraints may also have to be taken into account.

2. Ion–ion interactions and lattice geometry

2.1. Ion–ion interactions

2D lattices of ions can be used as a quantum simulator for many body spin-1/2 systems [24]. Forces such as the trapping potential, $F_T = -m\omega_i^2$, and the Coulomb force, $F_C = -e^2/(4\pi\epsilon_0 A^2)$, between the individual ions determine the equilibrium position. Laser beams or magnetic field gradients can be used to impart an additional force to the ions which displace the ion(s) depending on its internal state. This displacement leads to a change in the Coulomb force and thereby displaces the neighbouring ion(s) dependent on their own internal state. This state dependent coupling is given by [24]

$$J = \frac{\beta F^2}{m\omega^2},$$

(1)
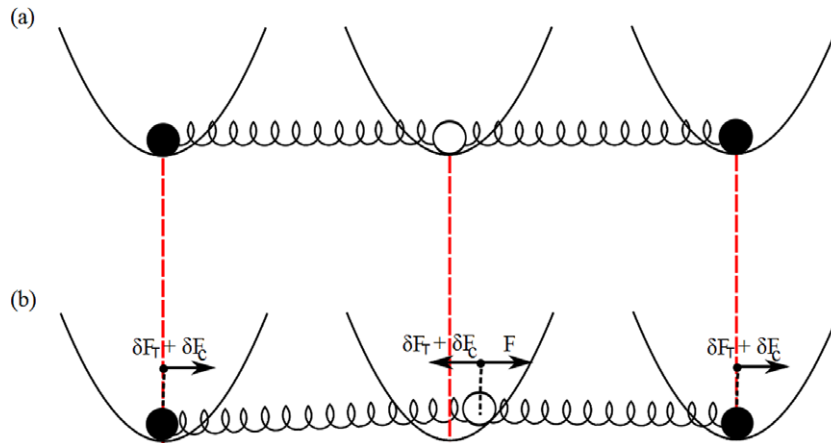
Figure 1. Pictorial diagram of three ions in adjacent traps. The ions feel a Coulomb force indicated by the springs between each ion and can be placed in two different states indicated by their colour. (a) Pictorial diagram showing the case with no state dependent force present. (b) Pictorial diagram showing how the system reacts to the presence of a state dependent force, F. Here the ions feel a change in the Coulomb force, δF_C, due to the displacement of the ions and a change in the restoring force, δF_T.

where m is the mass of an ion, F is the magnitude of the state dependent force applied to each ion and ω is the trap's secular frequency. We will consider how this force is applied later in the article. β is the ratio of the change in the Coulomb force to the change in the restoring force due to the displacement of the ions caused by the state dependent force and is given by [24]

$$\beta = \frac{e^2}{2\pi\epsilon_0 m \omega^2 A^3},\tag{2}$$

where A is the ion–ion spacing. There are two cases to consider, when $\beta > 1$ the change in the Coulomb force, δF_C, due to the displacement of an ion is dominant over the change in the restoring force, δF_T. This results in an interaction over a large number of trapping sites. When $\beta < 1$, the opposite is true resulting in an interaction which decays rapidly across the array. Trapping ions in a 2D array of microtraps makes it possible to satisfy the condition that $\beta < 1$ allowing systems with short range interactions to be simulated. An illustration of this system is shown in figure 1.

It is important to consider sources of decoherence when designing a 2D ion trap array. The internal state of an ion can remain coherent for tens of seconds [25, 26]. However, motional decoherence due to anomalous heating of ions will be an important factor during quantum operations within small scale ion traps as the implementation of spin dependent couplings involves the use of motional states of the ion. The coupling, J, will be observable if the coupling time, $T_J = 1/J$, is less than the motional decoherence time in the system and, therefore, the ratio of these two times is an important parameter of the system and is given by

$$K_{\text{sim}} = \frac{T_{\dot{n}}}{T_J},\tag{3}$$

where [18]

$$T_{\dot{n}} = \frac{4m\omega\hbar}{e^2 S_E(\omega)}. \tag{4}$$

Here $S_E(\omega)$ is the electric field noise density [13, 18]. In order for an interaction to occur on faster time-scales than the decoherence in the system, we require $K_{sim} > 1$ and it is the aim of the optimization process presented in this work to optimize the geometry in order to maximize this parameter. To acquire an understanding of how a geometry can affect K_{sim} it is necessary to determine its form with respect to the geometry variables. The form of T_J can be found by substituting equation (2) into (1) and is given by

$$T_J = \frac{2\pi\epsilon_0 m^2\omega^4 A^3\hbar}{e^2 F^2}. \tag{5}$$

The K_{sim} parameter can then be expressed as

$$K_{sim} = \frac{2F^2}{S_E(\omega)\pi\epsilon_0 m\omega^3 A^3}. \tag{6}$$

The secular frequency, ω, of a trapped ion [27] can be expressed as a function of α defined as

$$\alpha = \frac{V}{\Omega}, \tag{7}$$

where V is the amplitude of the rf voltage applied to the trap and Ω is 2π times the drive frequency in Hz, yielding,

$$\omega = \frac{eV\eta_{geo}}{\sqrt{2}m\Omega r^2} = \frac{e\alpha\eta_{geo}}{\sqrt{2}mr^2}, \tag{8}$$

where r is the height of an ion above the surface, e is the charge of an electron and η_{geo} is an efficiency factor which can range between 0 and 1 depending on the form of the geometry [27].

The secular frequency given in equation (8) can then be used along with $S_E(\omega) = \Xi r^{-4}\omega^{-1}$, where Ξ is a coefficient that can be experimentally obtained and depends on the temperature and surface of the trap electrodes (see [13] for a listing) to re-express equation (6) in the form

$$K_{sim} = \frac{4F^2 mr^8}{\Xi\alpha^2\eta_{geo}^2\pi\epsilon_0 A^3}. \tag{9}$$

To further understand how the geometry effects the K_{sim} value we will now introduce the parameters of a lattice geometry and relate them to equation (9).

2.2. Two-dimensional ion trap lattice geometry

A lattice is a regular tiling of a space by a primitive unit cell. Previous works [12, 21] concentrate on lattices created from square unit cells. In total there exist five types of cell which can be used to form a 2D lattice: centred rectangular, hexagonal and square as shown in figure 2, and rectangular and oblique [28]. The rectangular and oblique structures are not considered in this work due to their non-uniform ion–ion distances.

Figure 2 shows the polygon–polygon separation which is equal to the ion–ion distance, A, in equation (9). The polygon radius, R, along with the separation, will determine the height above the surface at which the ion is trapped, r, with larger polygon radii yielding higher ion heights. Another variable to be considered is the gap between the outer polygon in the array
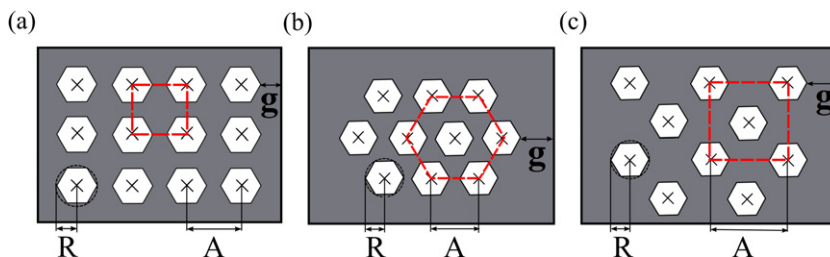
Figure 2. Diagrams showing the polygon radii R, the separation between the polygon centres, A, and the distance between the last polygon and the edge of the rf electrode (shown in grey), g. (a) Diagram showing a three by four ion trap surface array consisting of six sided polygons arranged with square unit cells. (b) Diagram showing a similar surface array arranged into hexagonal unit cells. (c) Diagram showing a surface array arranged into centred rectangular unit cells. The unit cells are indicated by dashed lines.

to the edge of the rf electrode, g. This can be used to alter the homogeneity of the individual trapping sites within the array. In general a non-homogeneous system results in spin dependent coupling rates which are a function of the lattice site, posing a significant problem for the scalability of such an array [29].

3. Simulation of lattices

To determine the electric field produced by a 2D array a method based on the Biot–Savart like law described by Oliveira and Miranda [30] was used. This method calculates the electric field produced by an arbitrarily shaped 2D electrode which is held at a potential V whilst the rest of the plane is held at a potential of zero. The electric field observed at a given point, $\overline{X}$, in space due to such an area held at a potential and bounded by a path C is given by [30]

$$E_{(\overline{X})} = \frac{V}{2\pi} \oint_C \frac{(\overline{x} - \overline{x}') \times d\overline{s}}{\left|\overline{x} - \overline{x}'\right|^3}, \tag{10}$$

where the curve, C, bounds the electrode and $\overline{x}'$ and $\overline{x}$ are vectors that locate the source point and field point respectively. By calculating the electric field in this manner an assumption is made that there is no gap between the areas held at the potential, V, and the areas held at zero. In microfabricated surface traps, gaps between the electrodes are required and typically range from 3 to 10 μm [13]. If, however, these gaps are small in comparison to the electrode structures they will not alter the trapping fields significantly [20, 31, 32]. The electric fields of individual electrodes can then be combined to determine potential nils and, therefore, trapping positions in the 2D trap arrays, using the numerical Gauss–Newton algorithm. The secular frequencies, trap depths and ion heights at these positions can then be determined.

To calculate the error of our numerical integration we compared simulations of five wire symmetric surface trap geometries with different central static electrode and rf rail widths in the gapless plane approximation using the method of Oliveira and Miranda [30] to results obtained with analytical equations described by House [31]. In all the geometries simulated the two rf rails were of equal width. Similarly to House, the outer static voltage electrodes were

IOP Institute of Physics **Φ** DEUTSCHE PHYSIKALISCHE GESELLSCHAFT

Table 1. Table showing the secular frequency, ω, and ion height, r, for different five wire surface trap geometries as calculated by the analytical method in House [31] and simulated by the method used in this work based on the Biot–Savart like law [30].

Electrode parameters				Simulations		House equations	
rf width (μm)	Central static electrode width (μm)	rf volt. (V)	rf freq. (MHz)	r (μm)	ω (MHz)	r (μm)	ω (MHz)
100	50	250	75	55.8	6.86	55.9	6.87
100	50	500	60	55.8	4.29	55.9	4.29
200	100	250	30	110.1	2.17	111.8	2.20
200	100	500	40	110.1	3.26	111.8	3.30
500	150	250	20	165.4	1.48	167.7	1.52
500	150	500	25	165.4	2.37	167.7	2.43

approximated as an infinitely long ground plane although the length of the inner rails were set to $3000\,\mu$m instead of infinite. A selection of these simulation results are shown in table 1.

In these results a general error for the ion heights and secular frequencies of less than 2 and 3% respectively was found, which leads to a maximum error in K_{sim} of 10%. For the following simulations it is therefore assumed that the maximum K_{sim} error is 10%. Additionally, numerical simulations of the geometries were carried out using methods described in [33], which indicate similar errors and trends for the ion height and secular frequency as the results obtained with the Biot–Savart like method.

4. Lattice geometry optimization

In this section we show how the parameters of the lattice geometry (discussed in section 2.2) can be optimized to achieve the highest possible K_{sim} value across the array for a given set of experimental parameters. To do this, we first show how to maximize the homogeneity of individual site properties over an array by varying the distance between the outer polygon in the array to the edge of the rf electrode, g, and show how this scales with lattice size. We will then use the homogeneous arrays to calculate the optimum number of sides, n, a polygon within the array should possess in order to maximize K_{sim}. We then outline a method for the optimization of the polygon radii, R, and separation, A, of an array and show how these vary with increased lattice size and ion mass.

4.1. Increasing the homogeneity of K_{sim} across the array

This is achieved by ensuring homogeneous secular frequencies, ion heights and trap depths across all the array sites. As shown in figure 3 the K_{sim} of trapping sites in an array can be altered to approach a common value if the distance, g, between the edge of the outer polygon and the edge of the rf electrode containing the polygon array is adjusted. As the value of g is increased, the K_{sim} value of the sites towards the centre drops, however, the outer sites K_{sim} value rises,
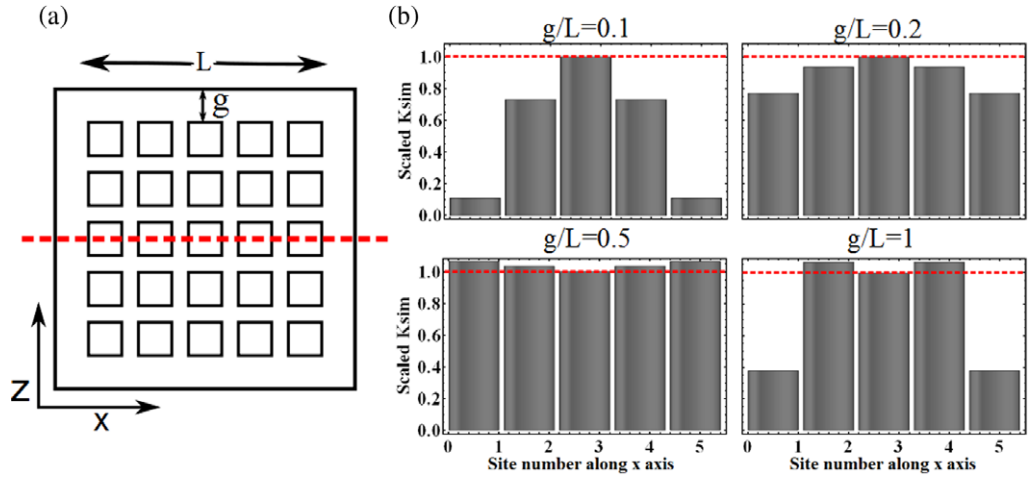
Figure 3. Diagram showing the effect of varying the distance g on the scaled K_{sim} value of the individual trapping sites. The K_{sim} values shown are scaled with that of the central site. (a) Representation of a 5×5 square type lattice array indicating the axis labelling. (b) Slices across the array (indicated by the dotted line in (a)) for g/L values of 0.1, 0.2, 0.5 and 1.

resulting in the properties converging towards each other. If the distance g is increased further beyond the point at which maximum homogeneity occurs the outer site properties drift away from those of the central sites and, therefore, decrease the homogeneity of the array.

To provide a value of g which is universal for all lattice sites, its value is given in units of lattice side length, L. The lattice side length is determined by the polygon separation, A, and radius, R, and can be expressed as

$$L = (M - 1)A + 2R, \tag{11}$$

where M is the number of lattice sites along one side of an array.

In order to quantify the array's homogeneity, H is defined as the average deviation of K_{sim} of each lattice site from the K_{sim} of the central site and is given by

$$H = \frac{1}{N} \sum_{n=1}^{N} \left| 1 - \frac{K_{sim_n}}{K_{sim_{centre}}} \right|, \tag{12}$$

where N is the total number of trapping sites in the lattice.

Figure 4 shows H for a 5×5 square type unit cell lattice for $0 < g/L < 1.5$. The maximum homogeneity, and thus the optimum g/L, is found when H is minimized. The error associated with H is given by

$$\sigma_H = \frac{\sqrt{N(\sigma_{K sim})^2 + N(\sigma_{K sim_{centre}})^2}}{N}, \tag{13}$$

where the error on all K_{sim} values is 10%, as shown in section 3. This yields an overall percentage error on H of $0.13/\sqrt{N}\%$.

Figure 5 shows the optimum g/L for hexagonal, central rectangular and square unit cell lattices of different sizes. The curves are found to be described by an equation of the form $g/L = a + bN^{-B}$ with a, b and B values for different lattice types shown in table 2. For large
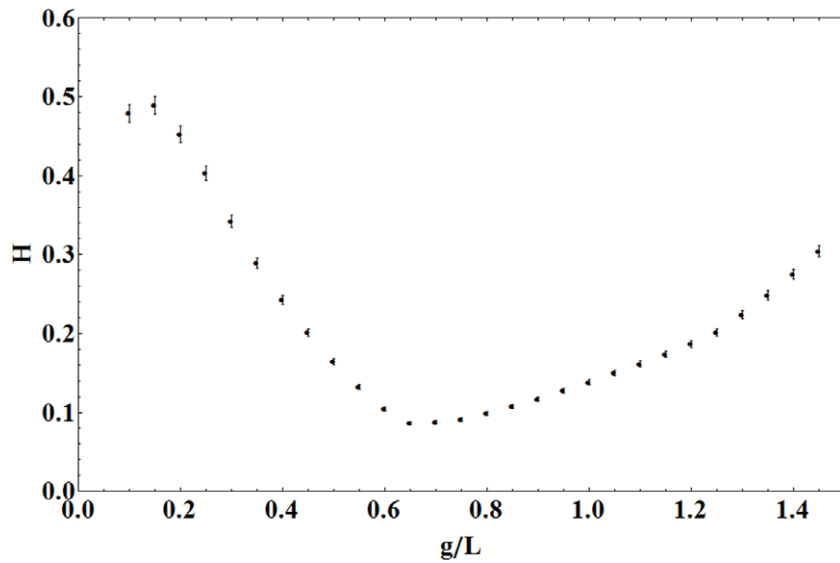
Figure 4. Graph showing the average deviation of the K_{sim} of each lattice site from the K_{sim} of the central site, H, for a 5×5 square type unit cell lattice for $0 < g/L < 1.5$. The error on H is given by $(0.13/\sqrt{N})H$ and the error of the minimum of H is determined by observing the spread of g/L which agrees, within error, with the minimum position.
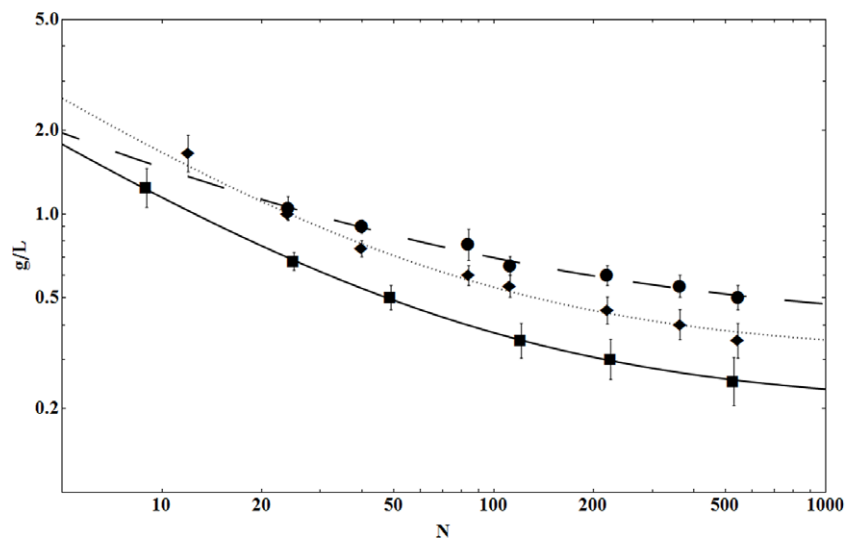
Figure 5. Graph showing the optimum g/L as a function of the total number of trapping sites, N, for square lattices (square markers), hexagonal lattices (circular markers) and centre rectangular lattices (diamond markers). The curves are given by $g/L = a + bN^{-B}$ with a, b and B values for different lattice types shown in table 2.

lattices, g/L is independent of N, as trapping sites close to the edge of the lattice are influenced only by the electric field created by that edge. In small lattices, however, the optimum g/L increases as the effect of the electric field from the opposite edge of the lattice increases.

Table 2. Table showing a and b values for the fits which describe g/L as a function of the number of sites in the lattice.

Lattice type	a	b	B
Square	0.20±0.01	5.21±0.38	0.74±0.03
Hexagonal	0.39±0.08	3.76±1.40	0.54±0.14
Centre rectangular	0.31±0.04	7.84±2.43	0.76±0.11
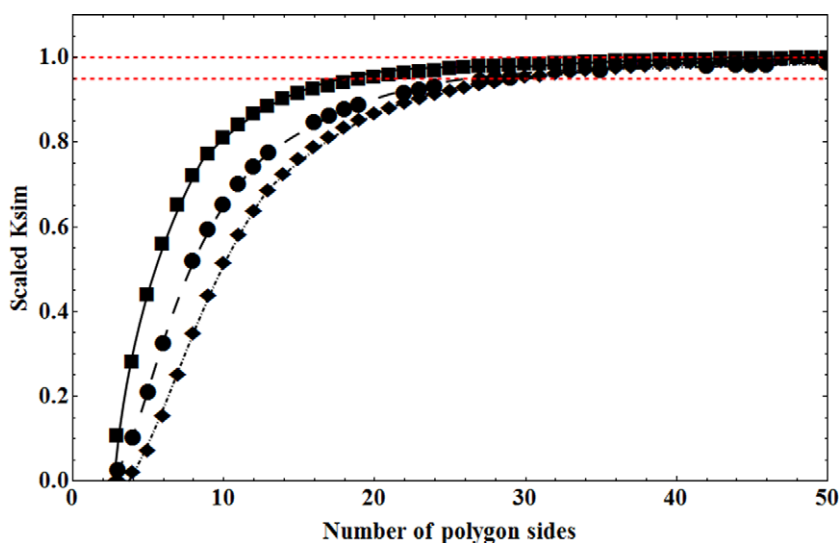
Figure 6. Graph showing the relationship between the number of polygon sides and K_{sim} for square (square markers), hexagonal (circular markers) and central rectangular (diamond markers) unit cell lattices. The dashed lines show the values of 1 and 0.95 of the scaled K_{sim} value.

4.2. Optimizing the number of polygon sides

We now investigate the optimum number of polygon sides, n, providing the highest K_{sim} value on the central trapping site (located above the central polygon) of a lattice.

To ensure the results are universal for all lattice geometries, g/L is set to the value which maximizes the homogeneity of each array, and all other parameters are scaled by normalizing K_{sim} to that of an identical geometry with polygons of 100 sides. This also allows comparison between the different types of lattices.

Figure 6 shows the scaled K_{sim} for the central site as the number of polygon sides is varied. As the number of sides is increased the value of K_{sim} approaches an asymptote, shown by the upper dashed line. This indicates that the best geometry will be made from circular electrodes. However, simulation times grow with increasing polygon side number and so it is advantageous to reduce this number to a minimum. It is shown that 95% of the maximum achievable K_{sim} (indicated by the lower dashed line) can be achieved with around $\geqslant$25–30 sides in the polygons.

4.3. Optimization method for polygon separation and radius

In this section we now maximize the K_{sim} of any arbitrary geometry. We will then go on and determine optimum geometries and show how they scale and, ultimately, are determined by $\alpha = V/\Omega$. We use the value of g determined in section 4.1 in order to provide the maximum K_{sim} homogeneity across the lattice, and set the number of sides to 25 as this provides a good approximation to the optimum circular geometry while keeping the simulation time at a minimum, as shown in section 4.2.

When considering any fixed arbitrary geometry, equation (9) shows that K_{sim} can be maximized by reducing the value of α. However, the minimum achievable α is limited by the lowest usable trap depth, as the trap depth is proportional to α^2 and is given by

$$T_D = \frac{\zeta e^2 \alpha^2}{\pi^2 m},$$ (14)

where e is the charge of an ion and ζ is a geometrical factor which is a function of A and R [31].

We will now focus on finding optimal geometries which we define as geometries that yield the highest value of K_{sim} for a given value of α. This will be carried out by fixing the trap depth at a reasonable minimum value (we use 0.1 eV for illustration purposes) which, as discussed above, provides the maximum K_{sim} for a given geometry, and then investigating the dependence of polygon radius, separation and ion height with α. To determine these dependences a K_{sim} contour plot is made by calculating the K_{sim} over a range of polygon separation, A, and radius, R, with a resolution of 1 μm. The range of polygon radius and separation used should not create traps with inter-well barriers of less than the minimum trap depth value, and to ensure this the polygon radius was kept to less than a third of the polygon separation. For each combination of polygon separation and radius a value of α is found which yields the minimum trap depth and, thus, maximizes the K_{sim} of the particular geometry. By following this method one can obtain the α required to achieve the minimum trap depth, the ion height, r, and K_{sim} for each geometry. From the resulting data the polygon separation and radius which yields the highest K_{sim} for a given α (the optimum geometry) can then be found. A graphical example of such data is shown in figure 7.

It can be seen from this method and the example data in figure 7 that the highest K_{sim} will be achieved with an infinite value of α, R and A. However, other effects may limit the magnitude of α. In order to determine a limit on α it is, therefore, necessary to describe the various array and trapping field dependent properties (such as secular frequency, ion height and K_{sim}) in terms of α.

By plotting these optimum parameters (polygon radius, separation and ion height) as a function of α, as shown in figures 8(a)–(c), linear relationships of the form
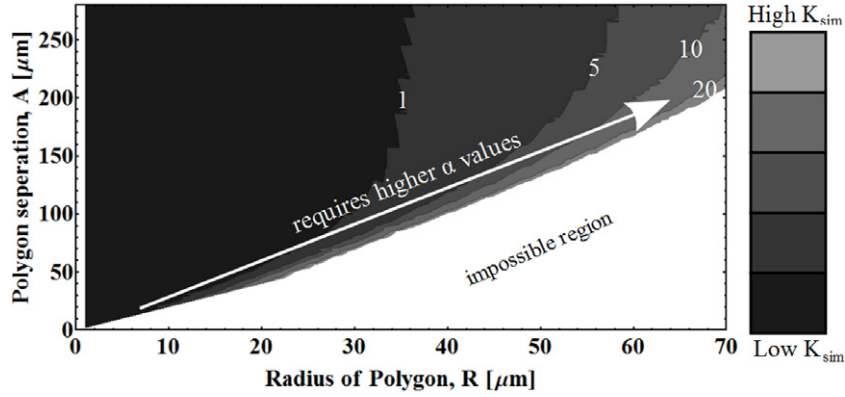
$$r = k_r \alpha,$$ (15)

$$A = k_A \alpha$$ (16)

and

$$R = k_R \alpha$$ (17)

are found for the optimal geometries. The values of k_r, k_A and k_R are dependent on the number of trapping sites in an array, as shown in figures 9(a)–(c) respectively, for lattices made from square type unit cells of polygons.

Figure 7. Example graph showing how the K_{sim} (absolute values indicated by numbers on contour lines) varies as a function of polygon radius and separation. The graph also indicates that the value of α increases as the radius and separation are increased. These data were obtained using the method described in section 4.3 with a polygon separation and radius resolution of $1\,\mu$m and a minimum trap depth of 0.1 eV. The value of α in the figure ranges from zero to $5/\pi$ V MHz^{-1}. The impossible region describes geometries where individual trapping sites start to combine to a single one and so possess a polygon radius, R, greater than or equal to a third of the polygon separation, A.

It is important to stress that equations (15)–(17) are only valid in the case of optimal geometries, which depend solely on α. With this in mind, it is now possible to re-express the secular frequency in equation (8) to describe the secular frequency of an optimized geometry as

$$\omega = \frac{e\eta_{\text{geo}}}{\sqrt{2}k_r^2 m\alpha}.$$ (18)

K_{sim} in equation (9) can also be re-expressed to describe that of an optimized geometry:

$$K_{\text{sim}} = \frac{4F^2 m k_r^8 \alpha^3}{\Xi\eta_{\text{geo}}^2 \pi \epsilon_0 k_A^3}.$$ (19)

Equation (19) shows that, for optimal geometries, K_{sim} is proportional to α^3 (as the value of α determines the electrode dimensions to be used) and so, to produce an array with a high K_{sim} for a given number of lattice sites (as k_r and k_A are functions of the number of trapping sites), a large value of α is preferable. Equations (16) and (17) show that the optimum geometry size is proportional to α. It, therefore, follows that larger lattice geometries will produce larger values of K_{sim}. This effect is illustrated in figure 7 which shows the K_{sim} as a function of polygon radius and separation. For optimized lattices, the optimal radius and separation will fall on a line described by $A = (k_A/k_R)\,R$, with higher values of α required for higher values of separation and radius as shown in equations (16) and (17) respectively.

The heating rate in ion traps has a strong dependence on the ion height ($\propto 1/r^4$) [18]. A large K_{sim} is achieved with large values of α, resulting in large ion heights, as shown in equation (15). It, therefore, can be concluded that a different scaling of the heating rate (for example in cryogenic systems) does not change the optimization process and optimal geometries.
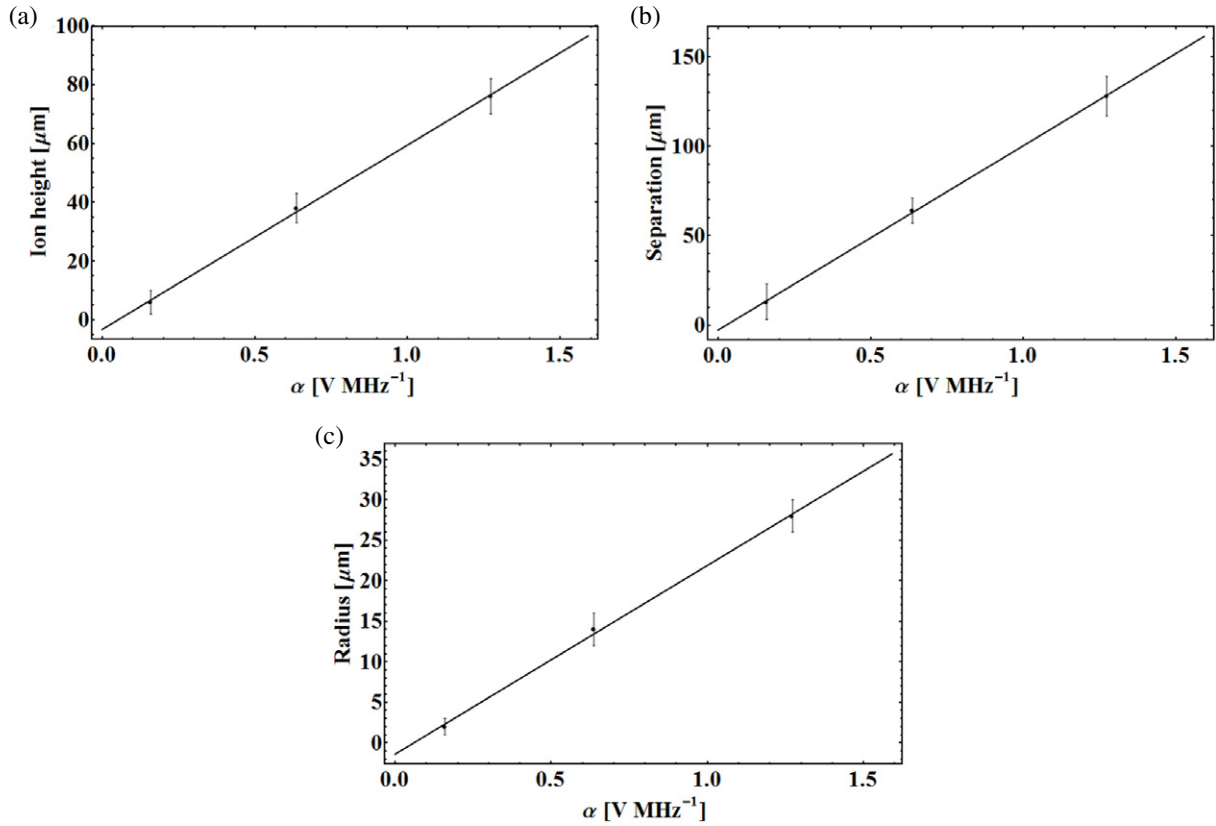
Figure 8. Graphs showing the ion height (a), polygon separation (b) and polygon radius (c) of an optimized lattice as a function of the ratio α. In all cases the plots are shown using $\alpha = V/\Omega$ where Ω is 2π times the drive frequency in Hz, and for arrays made from square type unit cells of polygons with 81 sites and for ^{171}Yb$^+$ ions.

It has now been shown that the optimal geometry for a given minimum trap depth and ion mass is determined solely by the value of α.

Optimal geometries and their K_{sim} values (in units of $1/\alpha^3$) can now be found by creating contour plots (such as shown in figure 7) for different values of lattice size, N, lattice unit cell type and ion mass, m. The error on the K_{sim} value, calculated from equation (9), was determined to be $\pm 10\%$ by comparing the secular frequency and ion heights obtained using the program with those predicted by House's analytical solutions for a five wire surface trap geometry [31].

5. Optimization results and analysis

In this section, optimum polygon separations, A, and radii, R, are obtained using the method outlined above for square, hexagonal and centre rectangular unit cell type lattices. These are shown as functions of lattice sizes and ion masses with the experimental constraint, α, scaled out. Throughout this optimization example, ^{171}Yb$^+$ ions will be used unless otherwise stated.

Figure 10 shows how the optimum scaled radius, R/α, and separation, A/α, of polygons vary as a function of lattice size for ^{171}Yb$^+$ ions. As explained in the previous section we
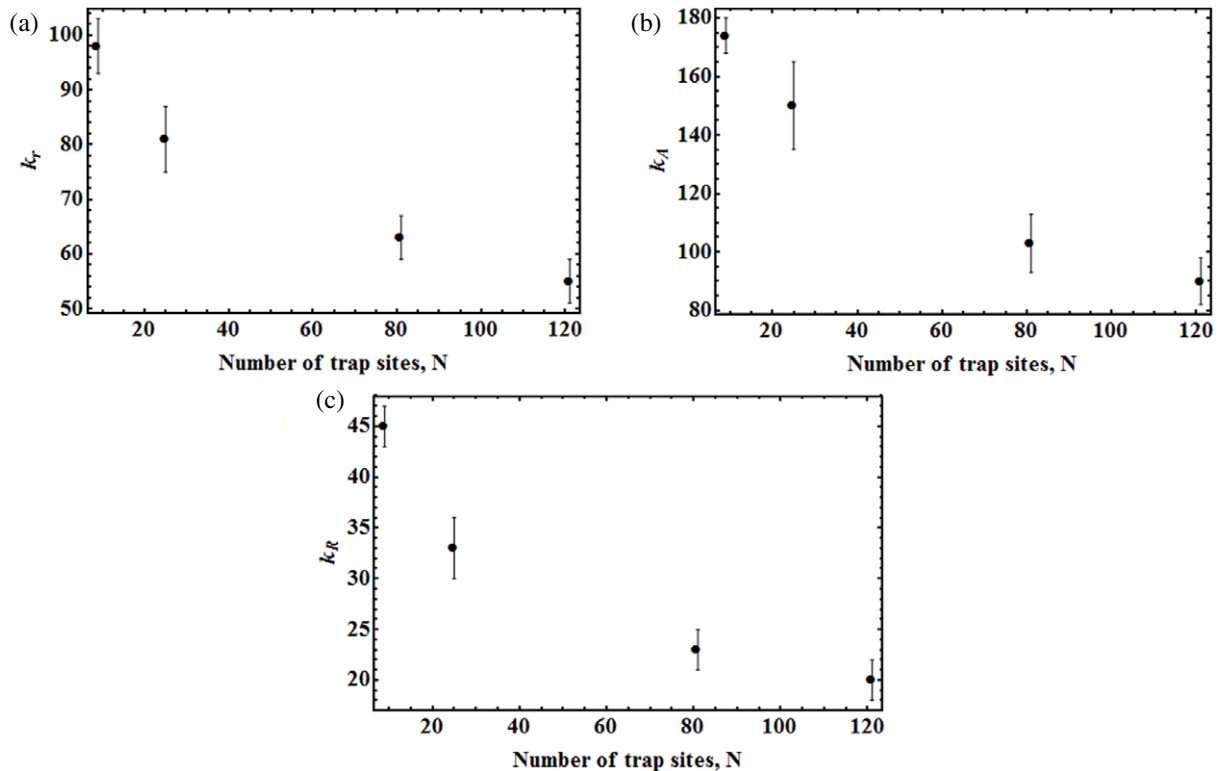
Figure 9. Graphs showing the value of k_r (a), k_A (b) and k_R (c) as a function of the number of trapping sites, N. In all cases the plots are shown using $\alpha = V/\Omega$ where Ω is 2π times the drive frequency in Hz and are for arrays made from square type unit cells of polygons using $^{171}\text{Yb}^+$ ions.
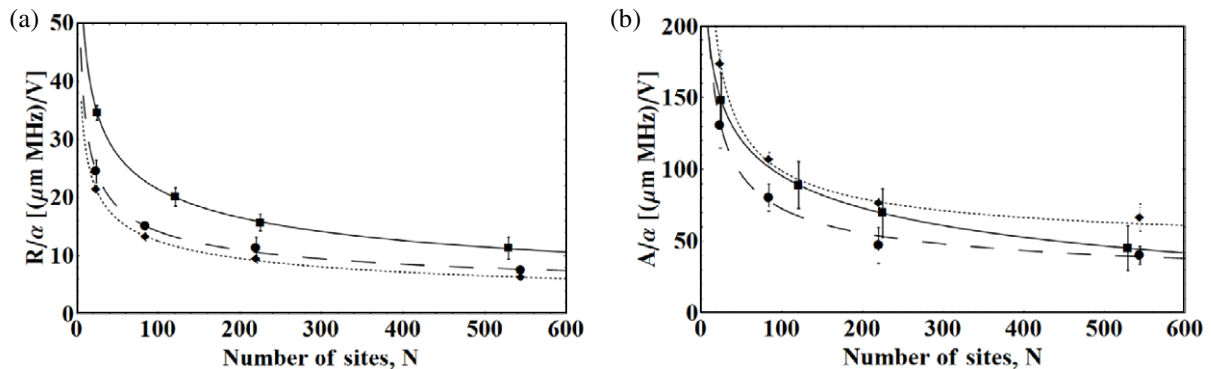
Figure 10. (a) Graph showing how the optimum polygon radius, R/α, varies as a function of the number of sites. (b) Graph showing how the optimum polygon separation, A/α, varies as a function of the number of sites. For both (a) and (b) the results shown are for square (square markers), hexagonal (circular markers) and centre rectangular (diamond markers) unit cell lattices with $^{171}\text{Yb}^+$ ions.

have assumed a minimum trap depth of $0.1\,\text{eV}$ for illustrative purposes. It can be seen from this figure that as the size of the lattice increases, the optimum polygon radius and separation asymptotically tend towards values representative of an infinitely large lattice. This is expected
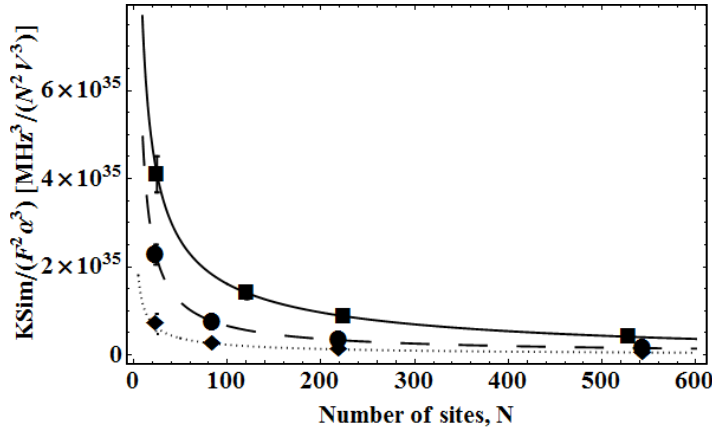
Figure 11. Graph showing how the optimum $K_{sim}/(F^2\alpha^3)$ varies as a function of the number of sites for optimum lattices with ^{171}Yb$^+$ ions. This is shown for square (square markers), hexagonal (circular markers) and centre rectangular (diamond markers) unit cell lattices. Here F is a state dependent force applied to the ions in the lattice.

Table 3. Table showing c, d and E values for the fits which describe R/α as a function of the number of sites in the lattice.

Lattice type	c	d	E
Square	-5 ± 1	101 ± 7	0.29 ± 0.03
Hexagonal	1 ± 3	85 ± 6	0.40 ± 0.08
Centre rectangular	-2 ± 2	68 ± 6	0.34 ± 0.05

as once a lattice becomes large enough, the addition of extra lattice sites will represent only a small change in the overall electrode geometry and, therefore, produce a small change in the electric field produced by the geometry. When the lattice is small however, additional lattice sites will represent a larger change in the geometry and will, therefore, cause a larger change in the electric field. Figure 11 shows how the scaled $K_{sim}/(F^2\alpha^3)$ scales as a function of the number of lattice sites, N, using scaled optimum polygon radii, R/α, and separations, A/α. The state dependent force F will be considered in more detail in section 6.2. Due to the dependence of K_{sim} on the geometry, the relationship between $K_{sim}/(F^2\alpha^3)$ and the number of sites is expected to be of similar form to that for optimal polygon radii, R/α, and separation, A/α, with the maximum $K_{sim}/(F^2\alpha^3)$ asymptotically tending towards a value representative of an infinitely large lattice.

Using the data shown in figures 10(a) and (b) and 11 the optimum radii and separation of the polygons as a function of number of sites, N, were found to follow a $c + dN^{-E}$ and $f + gN^{-G}$ relationship, respectively, while the maximum $K_{sim}/(F^2\alpha^3)$ follows a $k + lN^{-Q}$ trend. The values of c, d, E, f, g, G k, l and Q are shown in tables 3–5.

Using the data shown in figures 12(a) and (b) the optimum radii and separation of the polygons as a function of mass were found to follow a $o + pm^{-0.5}$ and $q + sm^{-0.5}$ relationship, respectively, with values of o, p, q and s shown in tables 6 and 7. Figure 13 shows how the optimum $K_{sim}/(F^2\alpha^3)$ varies as a function of the mass of the trapped ion, m, for 220 (square

Table 4. Table showing f, g and G values for the fits which describe A/α as a function of the number of sites in the lattice.

Lattice type	f	g	G
Square	-136 ± 7	457 ± 5	0.15 ± 0.01
Hexagonal	13 ± 24	547 ± 288	0.48 ± 0.21
Centre rectangular	40 ± 15	831 ± 282	0.57 ± 0.13

Table 5. Table showing k, l and Q values for the fits which describe $K_{\text{sim}}/(F^2\alpha^3)$ as a function of the number of sites in the lattice.

Lattice type	k	l	Q
Square	$-(2.69 \pm 2.97) \times 10^{34}$	$(3.09 \pm 1.31) \times 10^{36}$	(0.61 ± 0.13)
Hexagonal	$(0.52 \pm 6.00) \times 10^{33}$	$(3.51 \pm 1.54) \times 10^{36}$	(0.86 ± 0.12)
Centre rectangular	$-(3.09 \pm 6.12) \times 10^{35}$	$(5.23 \pm 5.11) \times 10^{37}$	(0.65 ± 0.26)
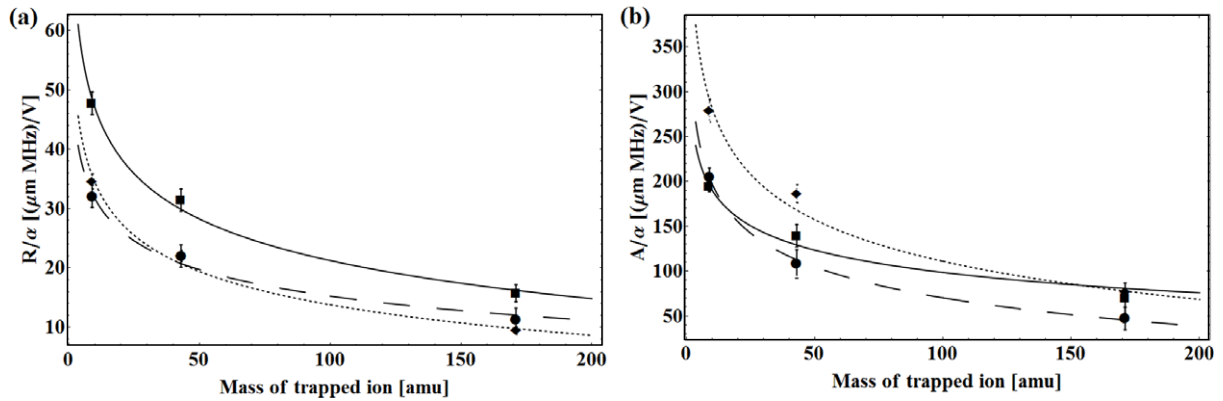
Figure 12. (a) Graph showing how the optimum polygon radius varies as a function of the ion mass for 220 (square type unit cells) and 225 (hexagonal and centre rectangular type unit cells) trapping sites. (b) Graph showing how the optimum polygon separation varies as a function of the ion mass. In both graphs this is shown for square (square markers), hexagonal (circular markers) and centre rectangular (diamond markers) unit cell lattices and the polygon radii and separations are scaled with α.

type unit cells) and 225 (hexagonal and centre rectangular type unit cells) trapping sites. It is found that the optimum $K_{\text{sim}}/(F^2\alpha^3)$ scales as $u + vm^{-0.5}$, with the values of u and v shown in table 8.

We note, as shown in figure 12, that as the mass of the ion is increased, the polygon radii and separation will have to be decreased in order to provide trapping regions with a depth of above 0.1 eV for a given α for 220 (square type unit cells) and 225 (hexagonal and centre rectangular type unit cells) trapping sites. It is also clear to see that ions with lighter masses will provide higher $K_{\text{sim}}/(F^2\alpha^3)$ values but will require larger lattice geometries compared to heavier ions.

Table 6. Table showing o and p values for the fits which describe R/α as a function of ion mass.

Lattice type	o	p
Square	-56 ± 6	138 ± 10
Hexagonal	-34 ± 7	88 ± 11
Centre rectangular	-48 ± 3	110 ± 6

Table 7. Table showing q and s values for the fits which describe A/α as a function of ion mass.

Lattice type	q	s
Square	-176 ± 47	489 ± 65
Hexagonal	-311 ± 15	678 ± 22
Centre rectangular	-402 ± 28	911 ± 51
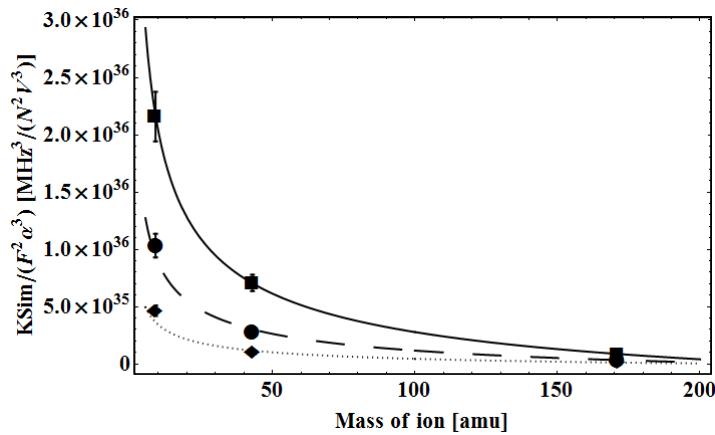
Figure 13. Graph showing how the optimum $K_{\mathrm{sim}}/(F^2\alpha^3)$ varies as a function of the ion mass for 220 (square type unit cells (circular markers)) and 225 (hexagonal and centre rectangular type unit cells (square markers and diamond markers respectively)) trapping sites.

6. Constraints on α

In this section we will discuss the considerations which could limit the value of α. To do this we will show how the power dissipation in a chip trap, the quantum simulation error and the interaction time vary as a function of α. This is important as from this a value of α can be determined for a given experiment, which will be shown in section 7.

6.1. Power dissipation in optimized arrays

The power dissipation of an ion trap chip is determined by the voltage, V, frequency, Ω, as well as the capacitance and resistance of the trap itself. This may, for a given capacitance and

Table 8. Table showing u and v values for the fits which describe $K_{sim}/(F^2\alpha^3)$ as a function of the ion mass.

Lattice type	u	v
Square	$-(5.25 \pm 3.00) \times 10^{35}$	$(7.96 \pm 1.72) \times 10^{36}$
Hexagonal	$-(1.25 \pm 0.60) \times 10^{35}$	$(5.08 \pm 1.29) \times 10^{36}$
Centre rectangular	$-(2.56 \pm 1.28) \times 10^{34}$	$(3.27 \pm 0.86) \times 10^{36}$

resistance, affect the value of α (the ratio between the rf voltage and drive frequency) which can be used. As the value of α is used to determine the optimum polygon radii and separation of a geometry, as shown in figure 10, for a given number of sites, N, and stability parameter, q, it is important to know how the power dissipation varies as a function of α.

The power dissipation of a chip is approximately given by [13]

$$P_D \approx \tfrac{1}{2} V^2 C^2 R \Omega^2, \tag{20}$$

where C and R are the capacitance and resistance of the chip. It is not possible to apply any combination of V and Ω to a geometry as they must be chosen so that the ion is stably trapped with a stability parameter given by [12, 27]

$$q = \frac{2e\eta_{geo}V}{mr^2\Omega^2} = \frac{2e\eta_{geo}\alpha}{mr^2\Omega} \tag{21}$$

between 0 and 0.9, where e is the charge of an electron.

The ion height, r, of ions trapped in the optimized lattices shown in this work have been found to be linearly proportional to α. This relationship is shown in figure 8(a) with the constant of proportionality, k_r, found to be $63(4)\,\mathrm{mV^{-1}\,s^{-1}}$ for the example case of square type lattice with 81 sites using $^{171}\mathrm{Yb}^+$ ions. Considering one particular ion height, r_0, and substituting for $r_0 = k_r\alpha_0$ and rearranging equation (21) for Ω yields

$$\Omega_0 = \frac{2e\eta_{geo}}{mk_r^2\alpha_0 q}. \tag{22}$$

This equation can be re-expressed for V_0 by noting that $V_0 = \Omega_0\alpha_0$:

$$V_0 = \frac{2e\eta_{geo}}{mk_r^2 q}. \tag{23}$$

Equations (22) and (23) show that, for a given ion mass, m, ion height, r_0, stability parameter, q, and number of trapping sites in the array (as k_r is a function of the number of trapping sites), there is one unique voltage, V_0, and unique parameter α_0. This means that a given ion height (and, therefore, a chosen value of α) determines both the voltage and drive frequency to be applied to the trap.

To express the power dissipation, P_D, in terms of α equations (22) and (23) can be substituted into equation (21) giving

$$P_D = \frac{8\eta_{geo}^4 e^4 C^2 R}{k_r^8 m^4 q^4 \alpha^2}. \tag{24}$$

Equation (24) shows that as α is increased, the power dissipated is reduced. This means that the power dissipation is low for high values of α and, as high values of α provide high values of

K_{sim} (see figures 11 and 13), power dissipation will not impact on producing high values of K_{sim} in optimized geometries. However, a low value of α will result in a high power dissipation in the chip and, so, the maximum allowable power dissipation in a chip will determine the lowest α which can be applied to a geometry.

6.2. Quantum simulation error

An upper limit on the value of α can be obtained from an estimation of the error of a quantum simulation using the method described in [34], where the error for the Ising model is given by

$$E_0 \approx \frac{1}{2}\eta^2 \sum_j (2\overline{n}+1) \left\langle \left[\left[O(t), \sigma_j^z(t) \right], \sigma_j^z(t) \right] \right\rangle. \tag{25}$$

Here $\overline{n}$ is the mean radial phonon number of the ions, O is the observable of the quantum simulation and η is a parameter which characterizes phonon displacement caused by the state dependent force and is given by [34]

$$\eta = \frac{F\sqrt{\hbar/(2m\omega)}}{\hbar\omega}, \tag{26}$$

where m is the mass of a trapped ion and $\omega/2\pi$ is its secular frequency.

If O is an M-site observable then there exist M non-vanishing commutators (for example a two-site correlation function ($M=2$) or a spin average ($M=1$)) and so the error on the simulation will not be dependent on the number of ions, N, in the array [34]. The error in equation (25) can now be re-written as

$$E_0 \approx \frac{F^2 M (\overline{n}+\frac{1}{2})}{2\hbar m\omega^3}. \tag{27}$$

Equations (19) and (27) show that both the K_{sim} and the error of the simulation, E_0, are proportional to the square of the state dependent force, F. It follows that the way in which this force is applied to the ions will determine the dependence of the simulation error on α. A discussion on the possible effects of the heating rate on the error can be found in appendix A. In this work we will consider applying this state dependent force via laser beams and magnetic field gradients.

To calculate the laser power required to achieve a force, F, it is assumed, for illustrative purposes, that the laser beam is focused to a sheet given by $25\,\mu$m multiplied by the width of the array. The laser intensity required to provide a state dependent force, F, can be provided by a laser beam of power, P. If the output power of the laser used is assumed to be constant, then the force applied to the ions will be dependent on α. This is because the lattice size will increase with increasing α and, therefore, so will the spatial area of the beam required to impart a force onto the ions. It is, therefore, required to express this force as a function of α. The intensity of a beam required to provide a state dependent force, F, is given by [35]

$$I_0 = \frac{3F\Delta\lambda I_{sat}}{2\pi\hbar\gamma^2}, \tag{28}$$

where Δ is the detuning of the laser from resonance, λ is the wavelength of the laser, I_{sat} is the saturation intensity of the ion and γ is 2π times the transition linewidth. The power of a laser beam is given by

$$P = I_0 a, \tag{29}$$

IOP Institute of Physics ✦ DEUTSCHE PHYSIKALISCHE GESELLSCHAFT

where a is the spatial area to which the beam is focused. In this work the beam is assumed to be focused to form a light sheet across the array with an area given by $a = (n_s - 1)AW = (n_s - 1)k_A\alpha W$, where n_s is the number of trapping sites (or polygons) along one side of the array and W is the width of the light sheet. By using equations (28) and (29) the force applied to the ions by a laser power, P, can be expressed as

$$F = \frac{2\pi\hbar P\gamma^2}{3a\Delta\lambda I_{\text{sat}}}. \tag{30}$$

The form of E_0 for the case of lasers applying the state dependent force can now be found by using equations (18), (30) and the general error equation (27) yielding

$$E_{0\text{laser}} = \frac{4\sqrt{2}}{9}\frac{\pi^2\hbar}{e^3}\frac{Mk_r^6\gamma^4 m^2 P^2\alpha(\overline{n}+\frac{1}{2})}{\eta_{\text{geo}}^3(n_s-1)^2 k_A^2 W^2\Delta^2\lambda^2 I_{\text{sat}}^2}. \tag{31}$$

It follows that both the K_{sim} and simulation error E_0 will decrease with increasing laser detuning, Δ. Therefore, the optimum detuning, for a given laser power and α, corresponds to the lowest detuning which provides the required K_{sim}. The optimum detuning to achieve the lowest simulation error for $^{171}\text{Yb}^+$ will be discussed in section 6.3.

Magnetic fields can also be used to provide the state dependent force, F, given by [4]

$$F_{\hat{i}} = \left(\frac{\hbar}{2}\right)\partial_i\omega\langle\sigma^{(\hat{i})}\rangle, \tag{32}$$

where $\omega = \gamma_g bi$ is the position dependent spin resonance frequency with $\gamma_g = e/m_e$ the gyromagnetic ratio and i is the x-, y- or z-direction. The magnetic field gradient b is assumed to arise from a magnetic field of the form $\overline{B} = \overline{B_0} + b\hat{i}$, where B_0 is a constant magnetic field offset. From this, the state dependent force, $F_{\hat{i}}$, produced from a magnetic field gradient, $b_{\hat{i}}$, is found to be

$$F_{\hat{i}} \approx \frac{\hbar e b_{\hat{i}}}{2m_e}, \tag{33}$$

where m_e and e are the mass and charge of an electron respectively. If one assumes the magnetic field is created by a current carrying wire located on the surface of a polygon, at a distance a from the centre of the polygon and making an angle of $45°$ with respect to the x-axis, then the magnetic field gradient will be of the form

$$b_{r'} = \frac{\mu_0 I}{2\pi r'^2}. \tag{34}$$

Here μ_0 is the permeability of free space, I is the current flowing through the wire and r'^2 is the distance squared of the ion from the current carrying wire and is equal to $r^2 + a^2$ where r is the ion height. We assume, for simplicity, that the distance a scales linearly with α with a constant of proportionality of k_a in order to keep the angle of r' to the x–z plane, θ, independent of α. As the ion height is known to scale linearly with α, from equation (15), it is possible to express the magnetic field gradient along r' as

$$b_{r'} = \frac{\mu_0 I}{2\pi\alpha^2\left(k_r^2 + k_a^2\right)}. \tag{35}$$

The component of this magnetic field gradient in the x–z plane can now be shown to be

$$b_{x,z} = \frac{\mu_0 I \cos\theta}{4\pi\alpha^2 \left(k_r^2 + k_a^2\right)}.$$ (36)

The form of K_{sim} for the case of magnetic field gradients applying the state dependent force can be found by using equations (18), (33), (36) and the general error equation (27) yielding

$$E_{0\text{mag}} = \frac{\sqrt{2}}{64} \frac{\hbar\mu_0}{\pi^2 m_e^2 e} \frac{k_r^6 m^2 I^2 \cos^2\theta M \left(\bar{n} + \frac{1}{2}\right)}{\eta_{\text{geo}}^3 \left(k_r^2 + k_a^2\right)^2 \alpha}.$$ (37)

Equations (31) and (37) show that the quantum simulation error is proportional to α for a state dependent force created by a laser beam and proportional to α^{-1} for a magnetic field gradient created by current carrying wires. For the case of laser beams the α scaling implies that as α is increased (yielding larger K_{sim} values and geometries as shown in section 4.3) the quantum simulation error will rise and, therefore, provide an upper limit on the value of α. For the magnetic field gradient case the upper limit on α comes from the current creating the gradient. While the α scaling for the quantum simulation error using magnetic field gradients implies that a larger α is advantageous, the current required to achieve a given magnetic field gradient scales as α^2 as can be deduced from equation (35). The maximum current that one can apply to the lattice therefore provides an upper limit for α.

It is also interesting at this point to note the different scaling with α of the laser and magnetic field gradient forces given in equations (30) and (32). The laser force can be seen to be $\propto \alpha^{-1}$ as it is a function of the inverse of laser sheet cross section, a, which is $\propto \alpha^1$. The magnetic gradient force, on the other hand, is $\propto \alpha^{-2}$ as it is a function of the magnetic field gradient $b_{r'}$, which is $\propto \alpha^{-2}$ due to r' having a linear relationship with α in the geometry considered.

6.3. Spontaneous emission

When applying the state dependent force to the ions using a laser beam additional decoherence will occur via spontaneous emission. The spontaneous emission rate is given by [36, 37]

$$S = \frac{\gamma g^2}{6} \left(\frac{1}{\Delta^2} + \frac{2}{(\Delta_{\text{fs}} - \Delta)^2} \right),$$ (38)

where γ is 2π times the linewidth in Hz, Δ is the laser detuning from resonance, Δ_{fs} is the fine structure splitting of the ion (approximately 100 THz for $^{171}\text{Yb}^+$) and g is the single photon Rabi frequency given by

$$g = \gamma \sqrt{\frac{I_0}{2I_{\text{sat}}}}.$$ (39)

Here, I_0 is the laser intensity and I_{sat} is the saturation intensity of the ion. It is possible to express the single photon Rabi frequency in terms of the laser power, P, by using equation (29) giving

$$g = \gamma \sqrt{\frac{P}{2(n_{\text{s}} - 1)k_A \alpha W I_{\text{sat}}}}.$$ (40)

It is now possible to describe an additional parameter, L_{sim}, which describes the ratio of interaction rate to the spontaneous emission rate as

$$L_{\mathrm{sim}} = \frac{T_S}{T_J}, \tag{41}$$

where

$$T_S = \frac{1}{S}. \tag{42}$$

It has been shown that the detuning which minimizes the effect of spontaneous emission is approximately 33 THz for ^{171}Yb$^+$ [38]. It, therefore, follows that the value of L_{sim} will be maximized with this detuning. This additional parameter is analogous to the parameter K_{sim} in equation (3) and is also required to be greater than unity, just like the original K_{sim}, when considering a state dependent force created using laser light. If magnetic field gradients are to be used to apply the state dependent force then L_{sim} is no longer relevant.

6.4. Other considerations

It is important to note here that an increase in α will increase the time taken for ion–ion interactions to take place in optimized lattice structures, as we will show in equation (44). Equation (5) gives an expression for the time taken for an ion–ion interaction to occur in any given fixed lattice structure. This can be expressed for optimized lattice structures by including the expressions for the ion–ion separation (polygon separation, A) and secular frequency, ω, from equations (16) and (18) respectively, to yield

$$T_J = \frac{e^2 \pi \epsilon_0 \hbar}{2} \frac{\eta_{\mathrm{geo}}^4 k_A^3}{k_r^8 F^2 m^2 \alpha}. \tag{43}$$

An expression to give the interaction time in optimized lattices as a function of α can now be arrived at by using equations (43) and (30),

$$T_J = \frac{9}{8} \frac{e^2 \epsilon_0}{\pi \hbar} \frac{\eta_{\mathrm{geo}}^4 k_A^3 ((n_s - 1) k_A W)^2 \Delta^2 \lambda^2 I_{\mathrm{sat}}^2 \alpha}{k_r^8 \gamma^4 P^2 m^2}. \tag{44}$$

Equation (44) clearly shows that as α is increased the time taken for an ion–ion interaction will increase and, so, it may be preferable to limit the magnitude of α after taking into account the effects on K_{sim}. A similar equation can also be derived for use with magnetic field gradients. It is also important to note here that increasing the laser power, P, will increase the value of L_{sim} as the spontaneous emission rate is proportional to P whereas the coupling rate is proportional to P^2 as shown in equations (38) and (44) respectively.

With the use of the equations derived in this section, optimal geometries can be calculated given certain experimental parameters and will be described in the following section.

7. Example case study

In this section, an example case will be presented to show how a 2D lattice for the use in quantum simulations can be designed using the work in this paper, whose successful operation is within reach of current technology when using lasers. We then go on to show that while

Table 9. Table summarizing the parameters for a 3×3 square type unit cell lattice at cryogenic temperature as shown in the example case study.

| α	R (μm)	A (μm)	Δ (THz)	P (W)	M	K_{sim}	L_{sim}	E_0
0.3	14	52	33	6.5	1	35	1.5	0.25

magnetic field gradients can be used to create a state dependent force their use may be more challenging.

From equation (23) we can see that there is a unique voltage for a given mass, m, lattice type and stability parameter, q. For this example case we choose a lattice comprised of square type unit cells with nine trapping sites for ^{171}Yb$^+$ ions with a stability parameter $q = 0.5$. Using these parameters the voltage can now be determined by calculating k_r. k_r can be found by plotting the ion height of an optimized lattice against α, as shown in figure 8(a), and finding the gradient of this linear relationship. For this example case $k_r = 98(5)$ mV^{-1} s^{-1}. Using this result and equation (23) we find the unique voltage to be 33(2) V where η_{geo} has been calculated to be 0.14(1).

The α dependent polygon radius and separation can be calculated by producing the corresponding graphs in figure 10, using the method described in section 4.3, for the lattice type and ion to be used. For this example case the optimum radius and separation of the polygons in terms of α are $45(1)\alpha$ and $174(1)\alpha$ μm respectively.

The next step is to choose a laser detuning from resonance and a maximum acceptable error, E_0, to be used. For ^{171}Yb$^+$, as explained in section 6.3, the optimum detuning is approximately 33 THz giving a wavelength of 355 nm, which is therefore used in this example case together with a maximum acceptable error of 0.25. Note that in this example case the array is assumed to be at cryogenic temperatures which correspond to an electric field noise density three orders of magnitude less than at room temperature. We can see from equation (31) that α needs to be minimized in order to keep the quantum simulation error low. The minimum α is determined by the lowest ion height one can easily achieve, which for this example case we choose to be equal to 30 μm. For this case we find $\alpha = 0.30(2)$ V MHz^{-1}. Having determined α we find the optimum radius and separation to be equal to 14(1) and 52(3) μm respectively. To calculate the laser power required equation (31) should be set to the maximum acceptable error and solved for the laser power, which is found to be 7(1) W assuming the ions to be cooled to $\bar{n} \ll 1$ and $M = 1$ (one site average observable). These conditions provide a coupling rate, J, of 530 ± 110 Hz with $\beta \approx (2.8 \pm 0.2) \times 10^{-5}$. This laser power can, for example, be achieved using a commercially available diode pumped solid state (coherent Paladin range) or fibre (coherent Talisker range) laser system. Table 9 summarizes all parameters for this example case study.

Figure 14 shows the effect a change of α and laser power, P, has on the quantum simulation error (solid curves), K_{sim} (dashed curves) and L_{sim} (dotted lines). The cross corresponds to the 2D lattice designed in this example case which represents the optimum case in terms of achieving the highest K_{sim} and L_{sim} for a maximum quantum simulation error of 0.25. We note that the main limitations in achieving lower quantum simulation errors stem from the lowest achievable ion height (lowest α) and magnitude of electric field noise density. Figure 14 also shows that higher values of K_{sim} and L_{sim} can be achieved with any given geometry (given by
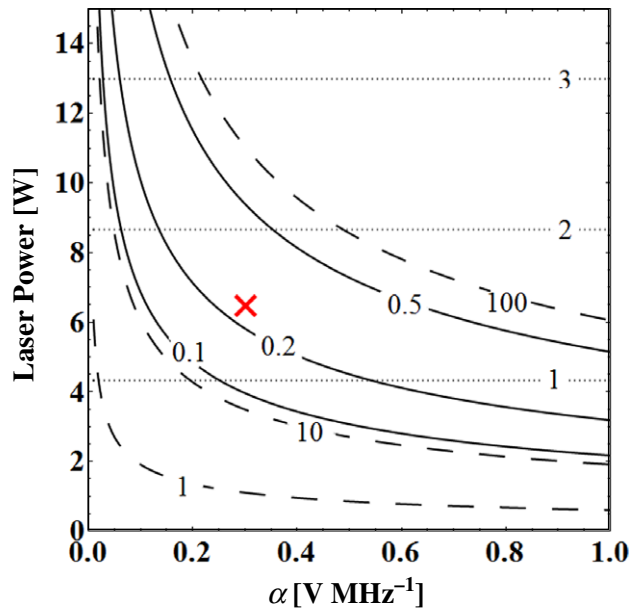
Figure 14. Graph showing the quantum simulation error (solid curves), K_{sim} (dashed curves) and L_{sim} (dotted lines) for a 3×3 square type unit cell lattice with $^{171}\text{Yb}^+$ ions as a function of α and laser power. Here traps are operated at cryogenic temperature. The cross indicates the example case.

the value of α) by simply increasing the power of the laser. However, this can only be achieved at the expense of higher quantum simulation errors.

State dependent forces can also be created using magnetic field gradients as described in section 6.2. Figure 15 shows the K_{sim} (solid curves) and the quantum simulation error (dashed curves) as a function of the magnetic field gradient, b, and α for traps operated at cryogenic temperature. Here we use $^{171}\text{Yb}^+$ ions in a 3×3 square unit cell array. As described in section 6.2, $E_0 \propto \alpha^{-1}$ indicating that a large α is advantageous. The limit on the maximum α is dependent on the maximum current one can apply to the geometry. Using equation (35) it is possible to calculate the current required to create a desired magnetic field gradient. In order to illustrate the magnitude of currents required we assume $k_a = k_r$, which will result in an angle $\theta = 45°$ (refer to section 6.2 for more information). We also set $\alpha = 0.30(2)\,\text{V}\,\text{MHz}^{-1}$, determined by the lowest achievable ion height which, for illustration purposes, we have set to $30\,\mu\text{m}$. The reason for choosing the minimum α value can be seen when considering equation (35) which clearly shows that, for a given magnetic field gradient, $I \propto \alpha^2$. In the magnetic field gradient case, the chosen α sets K_{sim} and E_0. For this case, again, we choose M = 1, $\bar{n} \ll 1$, $K_{\text{sim}} = 2$ and $E_0 = 0.01$ which requires a magnetic field gradient of $30\,500 \pm 3500\,\text{T}\,\text{m}^{-1}$ and is indicated by the cross in figure 15. This is achievable with a current of approximately 1200 A yielding a coupling rate, J, of 240 Hz and a $\beta = (2.8 \pm 0.2) \times 10^{-8}$. From this simple example case one can conclude that using magnetic field gradients to provide state dependent forces for use in quantum simulations using the methods and trap designs shown in this work is quite challenging. However, geometries trapping ions in chains allow for sizeable magnetic gradient induced couplings [39] and, so, a detailed investigation into optimizing the wires used for producing magnetic field gradients in the geometries discussed in this work could improve results.
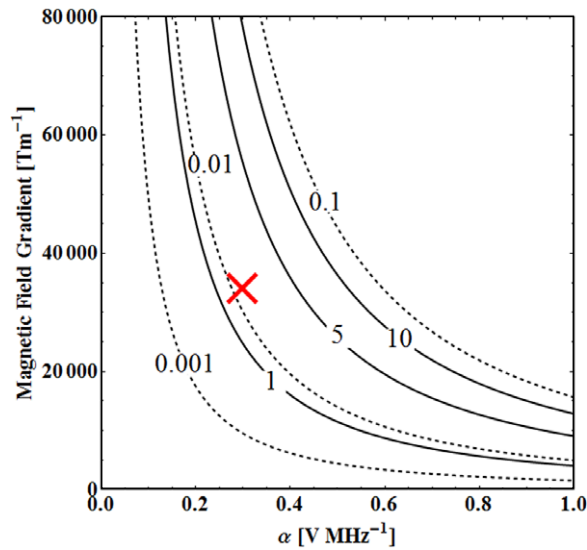
Figure 15. Graph showing the quantum simulation error (dashed curves) and the K_{sim} (solid curves) of a 3×3 square type unit cell lattice with ^{171}Yb$^+$ ions as a function of α and magnetic field gradient. Here traps are operated at cryogenic temperatures.

8. Conclusion

2D arrays of surface ion traps have the potential to provide a technology with which quantum simulations can be performed. In order for ion traps to be used successfully for this purpose a greater understanding is required of how the various geometry parameters affect the ions trapped above them. Throughout this work square, hexagonal and centre rectangular unit cell arrays of microtraps have been modelled in the gap-less plane approximation using the Biot–Savart like law in electrostatics [30]. Decoherence due to motional heating [18] was then compared to the ion–ion interaction [24] to provide a ratio used to describe how much faster an ion–ion interaction occurs in comparison to the motional decoherence, K_{sim}. This work investigates how various parameters in the array can be adjusted in order to optimize the device's ability to perform quantum simulations and shows how the interactions can be made as homogeneous as possible over the device. It has been shown how the homogeneity of the K_{sim} across an array can be altered by varying the distance from the outer polygon to the edge of the rf electrode. The distance required to maximize the K_{sim} homogeneity is also shown to vary as a function of the total size of the lattice. The number of polygon sides, n, required to maximize K_{sim} has also been found.

We have shown that the K_{sim} of a given lattice geometry can be maximized by reducing the value of α. However, as α reduces so does the trap depth. This results in the conclusion that the maximum K_{sim} of a geometry can be achieved by reducing the value of α until the trap depth reaches a reasonable minimum value.

Using this information, optimal geometries as a function of α are presented. This has been achieved by finding the relationships of polygon separation and radius with α for optimal geometries. It was found that, for these optimal geometries, K_{sim} scales as α^3. The individual polygon separation and radius were found to possess a linear relationship with α and, therefore,

IOP Institute of Physics **Φ** DEUTSCHE PHYSIKALISCHE GESELLSCHAFT

larger geometries have been found to produce larger values of K_{sim}. Therefore, the optimal lattice geometry is dependent solely on the value of α for a given ion mass and number of trapping sites in the array.

We presented a case study for determining an optimum geometry consisting of nine trapping sites arranged into square type unit cells for $^{171}Yb^+$ ions. We showed how the value of α can be chosen (and, therefore, the geometry dimensions) by taking into account the laser power (or static magnetic field gradient) required to produce a state dependent force acting on the ions, the K_{sim} and the error on the simulation. From this it has been found that to carry out quantum simulations with reasonable K_{sim} and error values it is preferable to use traps held at cryogenic temperatures as this reduces decoherence due to heating effects on the ions. Other methods known to significantly decrease the anomalous heating rate include pulsed laser electrode cleaning [40] and argon-ion beam electrode cleaning [41].

The scaling of anomalous heating has not yet been fully understood and is thought to possess a dependence on the ion height, r, of between r^{-4} and r^{-2}. In this work we have used r^{-4}, however, if the anomalous heating is found to possess a relationship with ion height nearer r^{-2} then the equations in this work can be adjusted and this is discussed in more detail in appendix B.

The relationships between lattice size and α with the polygon radii and separation obtained using the method described in this work will allow for the construction of 2D surface trap lattice arrays with high ratios of ion–ion interaction rates to decoherence rates, providing a system which could be used to perform quantum simulations.

Acknowledgments

Appendix A

The simulation error in equation (27) can be adjusted to take into account the heating of the ions during a simulation. If this occurs the mean radial phonon number $\bar{n}$ will become time dependent, $\bar{n}(t)$. It, therefore, follows that the error will also become time dependent and is given by

$$E_0(t) \approx \frac{F^2 M (\bar{n}(t) + \frac{1}{2})}{2\hbar m \omega^3}. \tag{A.1}$$

The time dependent mean radial phonon number will be a function of the heating rate $\dot{n}$, the interaction time, T_J, and the initial mean phonon number, $\bar{n}_0$, and is given by

$$\bar{n}(T_J) = \bar{n}_0 + \dot{n} T_J \tag{A.2}$$

yielding an error given by

$$E_0(T_J) \approx \frac{F^2 M (\bar{n}_0 + \dot{n} T_J + \frac{1}{2})}{2\hbar m \omega^3}. \tag{A.3}$$

It should be noted here that $\dot{n}T_J = 1/K_{sim}$ and so the error can be expressed as

$$E_0(T_J) \approx \frac{F^2 M(\bar{n}_0 + (1/K_{sim}) + \frac{1}{2})}{2\hbar m \omega^3}. \tag{A.4}$$

Equation (A.4) shows that as K_{sim} increases the error will tend towards that in equation (27) in section 6.2 for the case of $\bar{n} \ll 1$. This is because higher values of K_{sim} mean that less heating takes place during an interaction until the mean radial phonon number can be approximated as constant.

Appendix B

In the work presented we have used a motional heating rate, $\dot{n}$, which has an r^{-4} scaling, where r is the ion height. However the scaling of this anomalous heating has not yet been fully understood and so it is conceivable that a different scaling will be required to describe the effect. For this reason it is the aim of this appendix to outline the steps and main expressions required to obtain an optimized 2D ion trap array with an anomalous heating rate which possesses an arbitrary scaling with the ion height r^{-x}.

For the case of optimizing the homogeneity of K_{sim} across an array the results shown in section 4.1 will hold for any scaling of the heating rate with ion height. This is because this optimization aims to give each trapping site in the array the same properties and this is independent of the heating rate. The same applies to the optimization of the number of polygon sides described in section 4.2.

Equation (19) describing K_{sim} for an optimized geometry can be altered to take into account a different scaling of the heating rate with ion height. For an arbitrary scaling r^{-x} this equation can be expressed as

$$K_{sim} = \frac{4F^2 m k_r^{(4+x)} \alpha^{(x-1)}}{\Xi \eta_{geo}^2 \pi \epsilon_0 k_A^3}. \tag{B.1}$$

It can be seen in equation (B.1) that K_{sim} is proportional to $\alpha^{(x-1)}$. The values of k_r, k_A and k_R (described in section 4.3) are independent of the value of x and, so, the optimum geometry for a given α will be the same regardless of the scaling of the heating rate with ion height. Using this procedure optimum geometries can be computed for an arbitrary scaling of the anomalous heating with the ion height, r^{-x}.

References

[1] Cirac J I and Zoller P 2000 A scalable quantum computer with ions in an array of microtraps *Nature* **404** 579–81
[2] Kielpinski D, Monroe C R and Wineland D J 2002 Architecture for a large-scale ion-trap quantum computer *Nature* **417** 709–11
[3] Pons M, Ahufinger V, Wunderlich C, Sanpera A, Braungardt S, Sen(De) A, Sen U and Lewenstein M 2007 Trapped ion chain as a neural network: error resistant quantum computation *Phys. Rev. Lett.* **98** 023003
[4] Johanning M, Varn A F and Wunderlich C 2009 Quantum simulations with cold trapped ions *J. Phys. B: At. Mol. Opt. Phys.* **42** 154009
[5] Gerritsma R, Lanyon B P, Kirchmair G, Zähringer F, Hempel C, Casanova J, García-Ripoll J J, Solano E, Blatt R and Roos C F 2011 Quantum simulation of the Klein paradox with trapped ions *Phys. Rev. Lett.* **106** 060503

[6] Schneider C, Porras D and Schaetz T 2012 Experimental quantum simulations of many-body physics with trapped ions *Rep. Prog. Phys.* **75** 024401

[7] Kim K *et al* 2011 Quantum simulation of the transverse Ising model with trapped ions *New J. Phys.* **13** 105003

[8] Friedenauer A, Schmitz H, Glueckert J T, Porras D and Schaetz T 2008 Simulating a quantum magnet with trapped ions *Nat. Phys.* **4** 757–61

[9] Islam R *et al* 2011 Onset of a quantum phase transition with a trapped ion quantum simulator *Nat. Commun.* **2** 377

[10] Kim K, Chang M-S, Korenblit S, Islam R, Edwards E E, Freericks J K, Lin G-D, Duan L-M and Monroe C 2010 Quantum simulation of frustrated Ising spins with trapped ions *Nature* **465** 590–3

[11] Korenblit S *et al* 2012 Quantum simulation of spin models on an arbitrary lattice with trapped ions arXiv:1201.0776v1

[12] Clark R J, Lin T, Brown K R and Chuang I L 2009 A two-dimensional lattice ion trap for quantum simulation *J. Appl. Phys.* **105** 013114

[13] Hughes M D, Lekitsch B, Broersma J A and Hensinger W K 2011 Microfabricated ion traps *Contemp. Phys.* **52** 505–29

[14] Chiaverini J and Lybarger W E 2008 Laserless trapped-ion quantum simulations without spontaneous scattering using microtrap arrays *Phys. Rev.* A **77** 022324

[15] Mintert F and Wunderlich C 2001 Ion-trap quantum logic using long-wavelength radiation *Phys. Rev. Lett.* **87** 257904

[16] Ospelkaus C, Warring U, Colombe Y, Brown K R, Amini J M, Leibfried D and Wineland D J 2011 Microwave quantum logic gates for trapped ions arXiv:1104.3573v3

[17] Khromova A, Piltz Ch, Scharfenberger B, Gloger T F, Johanning M, Varn A F and Wunderlich Ch 2012 A designer spin-molecule implemented with trapped ions in a magnetic gradient *Phys. Rev. Lett.* **108** 220502

[18] Turchette Q A *et al* 2000 Heating of trapped ions from the quantum ground state *Phys. Rev.* A **61** 063418

[19] Schmied R, Wesenberg J H and Leibfried D 2009 Optimal surface-electrode trap lattices for quantum simulation with trapped ions *Phys. Rev. Lett.* **102** 233002

[20] Schmied R, Wesenberg J H and Leibfried D 2011 Quantum simulation of the hexagonal Kitaev model with trapped ions *New J. Phys.* **13** 115011

[21] Kumph M, Brownnutt M and Blatt R 2011 Two-dimensional arrays of radio-frequency ion traps with addressable interactions *New J. Phys.* **13** 073043

[22] Wunderlich H, Wunderlich C, Singer K and Schmidt-Kaler F 2009 Two-dimensional cluster-state preparation with linear ion traps *Phys. Rev.* A **79** 052324

[23] You-Yang X, Fei Z, Xiao-Long Z and Mang F 2010 Fast generation of cluster states in a linear ion trap *Chin. Phys.* B **19** 090317

[24] Porras D and Cirac J I 2004 Effective quantum spin systems with trapped ions *Phys. Rev. Lett.* **92** 207901

[25] Langer C *et al* 2005 Long-lived qubit memory using atomic ions *Phys. Rev. Lett.* **95** 060502

[26] Häffner H *et al* 2005 Robust entanglement *Appl. Phys. B: Lasers Opt.* **81** 151–3

[27] Madsen M J, Hensinger W K, Stick D, Rabchuk J A and Monroe C 2004 Planar ion trap geometry for microfabrication *Appl. Phys.* B **78** 639

[28] Kittel C 1996 *Introduction to Solid-State Physics* (New York: Wiley)

[29] Mc Hugh D and Twamley J 2005 Quantum computer using a trapped-ion spin molecule and microwave radiation *Phys. Rev.* A **71** 012315

[30] Oliveira M and Miranda J A 2001 Biot–Savart-like law in electrostatics *Eur. J. Phys.* **22** 31–8

[31] House M G 2008 Analytic model for electrostatic fields in surface-electrode ion traps *Phys. Rev.* A **78** 033402

[32] Amini J M, Uys H, Wesenberg J H, Seidelin S, Britton J, Bollinger J J, Leibfried D, Ospelkaus C, VanDevender A P and Wineland D J 2010 Toward scalable ion traps for quantum information processing *New J. Phys.* **12** 033031

[33] Singer K, Poschinger U, Murphy M, Ivanov P, Ziesel F, Calarco T and Schmidt-Kaler F 2010 Colloquium: trapped ions as quantum bits: essential numerical tools *Rev. Mod. Phys.* **82** 2609–32

[34] Deng X-L, Porras D and Cirac J I 2005 Effective spin quantum phases in systems of trapped ions *Phys. Rev. A* **72** 063407

[35] Haljan P C, Brickman K-A, Deslauriers L, Lee P J and Monroe C 2005 Spin-dependent forces on trapped ions for phase-stable quantum gates and entangled states of spin and motion *Phys. Rev. Lett.* **94** 153602

[36] Ozeri R *et al* 2007 Errors in trapped-ion quantum gates due to spontaneous photon scattering *Phys. Rev. A* **75** 042329

[37] Wineland D J *et al* 2003 Quantum information processing with trapped ions *Phil. Trans. R. Soc.* **361** 1349

[38] Campbell W C, Mizrahi J, Quraishi Q, Senko C, Hayes D, Hucul D, Matsukevich D N, Maunz P and Monroe C 2010 Ultrafast gates for single atomic qubits *Phys. Rev. Lett.* **105** 090502

[39] Welzel J, Bautista-Salvador A, Abarbanel C, Wineman-Fisher V, Wunderlich C, Folman R and Schmidt-Kaler F 2011 Designing spin–spin interactions with one and two dimensional ion crystals in planar micro traps *Eur. Phys. J.* D **65** 285–97

[40] Allcock D T C, Guidoni L, Harty T P, Ballance C J, Blain M G, Steane A M and Lucas D M 2011 Reduction of heating rate in a microfabricated ion trap by pulsed-laser cleaning *New J. Phys.* **13** 123023

[41] Hite D A, Colombe Y, Wilson A C, Brown K R, Warring U, Jördens R, Jost J D, Pappas D P, Leibfried D and Wineland D J 2011 Reduction of anomalous heating in an in-situ-cleaned ion trap arXiv:1112.5419v1